Trypanosomal Nucleoside Hydrolase. A Novel Mechanism from the Structure with a Transition-State Inhibitor†

Massimo Degano,‡ Steven C. Almo, James C. Sacchettini,*,§ and Vern L. Schramm*

Department of Biochemistry, Albert Einstein College of Medicine, Bronx, New York 10461

Received December 8, 1997; Revised Manuscript Received February 26, 1998

ABSTRACT: Nucleoside N-ribohydrolases are targets for disruption of purine salvage in the protozoan parasites. The structure of a trypanosomal N-ribohydrolase in complex with a transition-state inhibitor is reported at 2.3 Å resolution. The nonspecific nucleoside hydrolase from *Crithidia fasciculata* cocrystallized with *p*-aminophenyliminoribitol reveals tightly bound Ca^{2+} as a catalytic site ligand. The complex with the transition-state inhibitor is characterized by (1) large protein conformational changes to create a hydrophobic leaving group site (2) C3′-exo geometry for the inhibitor, typical of a ribooxocarbenium ion (3) stabilization of the ribooxocarbenium analogue between the neighboring group 5′-hydroxyl and bidentate hydrogen bonds to Asn168; and (4) octacoordinate Ca^{2+} orients a catalytic site water and is liganded to two hydroxyls of the inhibitor. The mechanism is ribooxocarbenium stabilization with weak leaving group activation and is a departure from glucohydrolases which use paired carboxylates to achieve the transition state.

INTRODUCTION

Enzymatic cleavage of the N-ribosidic bonds of nucleosides, nucleotides, cofactors, RNA, and DNA is essential for normal metabolic function in all organisms. Hydrolytic reactions release the aglycone in DNA repair and tRNA modification (*1*, *2*), are essential for the pathways of nucleoside salvage in protozoan parasites (*3*, *4*), and are responsible for the action of ribosome-inactivating toxins, of which ricin is one example (*5*, *6*). N-ribosyl transferases are also members of this group and include cholera, pertussis, and diphtheria toxins which ADP-ribosylate G-proteins and transcription factors (*7*). Also related are the signal transduction proteins such as CD38, which form and hydrolyze cyclic-ADP-ribose as a Ca^{2+} flux regulator in cell development (*8*). Purine nucleoside phosphorylase is an essential mammalian enzyme capable of phosphorolysis or hydrolysis of the same carbon−nitrogen bonds (*9*, *10*). Several of these enzymes have been characterized by structural studies (*11*−*18*), and others have been among the first enzymes to have their transition-state structures established by kinetic isotope effect studies (*19*−*24*). However, there has been no crystal structure of an N-ribosyl hydrolase in a transition-state complex. The purpose of this report is to characterize a member of the N-ribohydrolases in a complex with a transition-state analogue. The 1-substituted iminoribitols are powerful inhibitors for some of these enzymes (*25*, *26*). The atomic structure of nucleoside hydrolase complexed with *p*-aminophenyliminoribitol (pAPIR) reveals the structural basis for tight binding of the transition-state complex.

The inosine-uridine preferring nucleoside hydrolase (IU-NH) from *Crithidia fasciculata* catalyzes the N-ribosyl hydrolysis of all commonly occurring purine and pyrimidine nucleosides via an oxocarbenium-ion transition state (Figure 1). It is the most extensively characterized of the N-ribosyl hydrolases (*20*, *25*, *27*−*34*). IU-NH is involved in the purine salvage pathways of protozoan parasites and has not been found in mammals, since higher eukaryotes release the purine ring of nucleosides by the phosphorolysis catalyzed by purine nucleoside phosphorylase. Protozoan parasites lack de novo purine biosynthetic pathways, making them completely dependent on exogenous purines salvaged from the hosts (*3*). Inhibitors specific for enzymes of purine salvage are under consideration as antitrypanosomals. Analogues that resemble both the geometric and electronic properties of the transition state have been synthesized and have proven to be powerful competitive inhibitors of IU-NH, displaying inhibition constants to 2 nM (*26*, *32*). The complex with *p*-aminophenyliminoribitol (pAPIR, Figure 1) is characterized by a dissociation constant of 30 nM (*25*). The structure of IU-NH with pAPIR is compared to the structure of the unliganded enzyme to provide information on the conformational changes in the enzyme as it is converted from the unliganded state to the transition state (*35*). Active-site elements in contact with the transition-state inhibitor identify the mechanism of transition-state stabilization.

MATERIALS AND METHODS

Crystallization. The enzyme was purified from *Escherichia coli* bearing the pET3d-IUNH plasmid encoding for IU-NH from *C. fasciculata* (*34*). Crystals of the IU-NH/pAPIR complex were obtained at room temperature with the hanging

† The work was supported by Research Grant GM41496 from the National Institutes of Health and by the G. Harold and Leila Y. Mathers Charitable Foundation.

* Corresponding authors. Tel: (718) 430-2813. Fax: (718) 430-8565. E-mail: vern@aecom.yu.edu.

‡ Present address: Department of Molecular Biology, The Scripps Research Institute 10550 North Torrey Pines Road, La Jolla, CA 92037.

§ Department of Biochemistry and Biophysics, Texas A&M University, College Station, TX 77843.

S0006-2960(97)03012-2 CCC: $15.00
Published on Web 04/16/1998

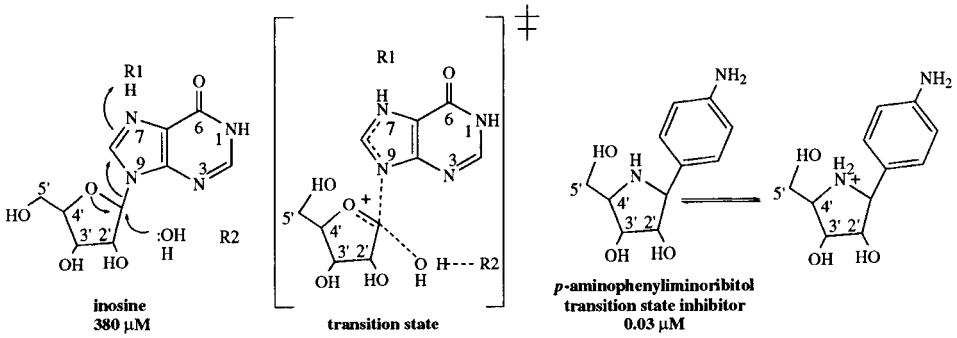

FIGURE 1: Nucleoside depurination reaction catalyzed by the nonspecific IU-NH. The structure of the transition state includes protonation of the leaving group, oxocarbenium ion character in the ribose, preassociation of the water nucleophile and reorientation of the 5′-hydroxyl. Features of the transition state are based on analysis of kinetic isotope effects (*20*). The 1′-substituted iminoribitols are transition-state inhibitors and bind to the enzyme with the imino nitrogen in the unprotonated state (*29, 58*). Mutagenesis and substrate specificity studies have implicated His 241 as the group which neutralizes the hypoxanthine leaving group (*34*).

drop vapor diffusion method, from 1.8 M ammonium sulfate and 3% 2-propanol. The enzyme, 34 mg/mL (~1.0 mM subunits, ~0.25 mM tetramer) in 10 mM triethanolamine pH 7.0, was incubated with 4 mM inhibitor at 4 °C for 30 min prior to mixing with an equal volume of precipitant solution. The crystals belong to the orthorhombic crystal system, space group *I*222. The unit cell parameters are $a = 120.04$ Å, $b = 158.53$ Å, $c = 205.37$ Å, $\alpha = \beta = \gamma = 90°$. The crystals contain one IU-NH tetramer per asymmetric unit with 65% solvent, ($V_m = 3.58$ Å^3/Da).

Data Collection. X-ray diffraction intensities were collected from single crystals at room temperature on a Siemens ×1000 area detector coupled to a Rigaku rotating anode X-ray generator operating at 55 kV and 85 mA. A graphite monochromator was used to select for the CuKα radiation (1.5418 Å). A 2.75 Å resolution data set was collected and allowed the solution of the structure of the complex. A second, higher quality and better resolution data set was collected and used for the refinement of the structure. Data indexing was performed using SADIE, while data integration, reduction, and scaling were performed using SAINT (*36*).

Structure Determination. The structure was solved by molecular replacement using the program AMoRe (*37, 38*). The dimer found in the orthorombic crystals of the unliganded IU-NH was used as the search model (PDB accession code 1MAS), after resetting the temperature factors of all atoms to 20.0 Å^2 and removing all water molecules and ions from the model. Two rotation function solutions were found, corresponding to the orientations of the two homodimers that constitute the tetrameric, active IU-NH. From the results of the translation function, the correct space group was determined to be *I*222, based on the differences in correlation coefficients between solutions in the two space groups. At this stage, 7% of the measured unique reflections equally sampled in resolution ranges, corresponding to 6118 reflections, were set aside for cross-validation (*39*). Rigid body refinement of the four IU-NH subunits resulted in values of 37.3% for R_{crys} and 39.2% for R_{free} using all reflections between 8.0 and 2.8 Å. A simulated annealing procedure from 4000 K as implemented in X-PLOR (*39, 40*), restraining noncrystallographic symmetry by applying a harmonic strength constant of 300 kcal/(mol Å^2), was followed by an overall temperature factor and individual temperature factor refinement. This resulted in a decrease of R_{crys} and R_{free} to 0.22 and 0.25, respectively. SIGMAA-weighted $2F_o - F_c$ and $F_o - F_c$ omit maps (*41*), calculated after omitting 10% of the model, and simulated annealed omit maps were inspected for manual adjustment of the protein model, using the program O (*42*). A macrocycle of refinement, consisting of manual adjustment of the model followed by positional refinement and restrained individual *B* factor refinement, was considered successful only if it resulted in a decrease in R_{free}. Amino acid residues 78−83, missing in the unliganded structure (*35*), were unambiguously identified in difference maps and included in the model. The resolution was then extended to 2.3 Å and four inhibitor molecules, one per monomer in the asymmetric unit, were added to model. Application of a solvent mask, as implemented in X-PLOR, allowed the productive inclusion of the low-resolution data, resulting in significantly improved electron density maps and in a decrease of R_{free} by 2.0%. The last stage of refinement resulted in final values for the crystallographic validators R_{crys} and R_{free} of 20.5 and 23.4%. In the final model, 313 amino acid residues of each IU-NH monomer have been included, as well as four inhibitor and 158 ordered water molecules. Analysis of the final model with PROCHECK (*43*) shows 87.7% of the residues in the most favorable regions, 11.5% in additionally allowed regions, 0.7% in generously allowed regions, and no residues in unfavorable regions. The rms error on the coordinates, estimated from a cross-validated Luzzati plot (*44*) is 0.35 Å.

Ca^{2+} Analysis. Enzyme was passed through a Sephadex G-25 column previously equilibrated with 50 mM triethanolamine, pH 8.0, or 20 mM HEPES, pH 7.5, containing 0.1 mM EDTA and 0.1 mM dithiothreitol. The peak protein fractions and fractions containing no enzyme were analyzed for 20 metal ions by plasma emission spectroscopy at the Chemical Analysis Laboratory, University of Georgia. Several enzyme samples have been analyzed and contain 0.6−1.3 mol of Ca/mol IU-NH subunit. None of the other of 19 elements in this analysis were present at more than 0.1 mol/mol of enzyme except those present as counterions for the buffer.

RESULTS AND DISCUSSION

Structure of the IU-NH/pAPIR Complex. The structural determination of the complex between IU-NH and pAPIR was performed by molecular replacement using the coordinates of the native IU-NH as a search model (*35*) (Table 1). The structure of the complex has been refined to a nominal

Table 1: Data Collection, Structure Determination, and Refinement Statistics

Data Collection					
data set	resolution (Å)	unique reflections	completeness (%)	$<I/\sigma(I)>$	R_{symm}[a] (%)
native 1	2.75 (3.0−2.75)	49 457	92.4 (82)	5.90 (1.9)	7.5
native 2	2.3 (2.4−2.3)	73 166	80.8 (75)	9.31 (2.2)	8.2

Molecular Replacement	
rotation function:	
resolution range (Å)	12.0−4.0
integration radius (Å)	25.0
dimer 1 RF/σ(RF) value	9.7
dimer 2 RF/σ(RF) value	9.1
first noise peak	4.1
translation function	
resolution range (Å)	8.0−5.0
dimer 1 correlation coefficient	23.9
(first noise peak)	20.6
dimer 2 correlation coefficient	43.4
(first noise peak)	24.0

Refinement Statistics	
resolution range (Å)	25.0−2.3
R_{crys}[b]	0.204
R_{free}[b]	0.234
Rms deviation from ideal geometry	
bond lengths (Å)	0.011
bond angles (deg)	1.8
b factors (Å^2)	3.1

[a] $R_{symm} = \sum_h\sum_i |I(h) - I_i(h)|\sum_h\sum_i I_i(h)$ where $I_i(h)$ and $I(h)$ are the ith and mean intensity values of reflection h, respectively. [b] $R = \sum_h||F_o| - |F_c||/\sum_h|F_o|$ where F_o and F_c are the observed and calculated structure factor amplitudes of reflection h, respectively. The sum is extended over all unique reflections for R_{cryst}, while for R_{free} the sum is over a subset of reflections excluded from all stages of refinement.

resolution of 2.3 Å to values of $R = 0.205$ and $R_{free} = 0.234$ for these crystallographic validators. The inhibitor is bound at the C-terminal end of the core eight-stranded β-sheet of IU-NH (Figure 2). Upon binding the inhibitor, IU-NH undergoes structural changes which bring protein residues into the binding site and restricts the access to the solvent (Figure 2). The root-mean-square deviation for backbone atoms between the unliganded and liganded protein is 1.07 Å, but decreases to 0.61 Å when the three segments that undergo conformational change are removed from the calculation. The two rmsd values were computed over residues 2−37, 43−74, 83−318, 94−164, 169−220, and 240−314, from models of the native enzyme and the IU-NH/pAPIR complex. The average temperature factors for the two polypeptide chains found in the asymmetric unit of unliganded IU-NH are 18.0 and 38.0 Å^2, respectively, indicating higher disorder for one subunit (*35*). In the complex with pAPIR, the mean temperature factors of the four subunits are homogeneous, their values averaging 29.3 Å^2.

The loop (C1 of Figure 2) connecting strand β2 to helix α2 (residues 38−42) closes toward the interior of the occupied binding cavity, placing the side chain of Asn 39 3.1 Å from the O2′ hydroxyl of the iminoribitol (Figures 3 and 4). The movement of this loop is obtained by a rotation hinged about Gly 38 that propagates to residue Thr 42. Two ordered solvent molecules in the unliganded structure are replaced by the side-chain amide nitrogens of Asn 39 and Gln 40. A second structural change involves the amino acid residues 166 through 170 in the short α5 segment (C2 of Figure 2), which brings the aromatic rings of Phe 167 and pAPIR roughly perpendicular to each other. The side chain atoms of Asn 168 also rearrange to hydrogen bond to the O3′ hydroxyl and the N4′ imino group of the inhibitor. The position of Glu 166 is unchanged from the native enzyme, but forms a 2.5 Å hydrogen bond to the iminoribitol O5′ hydroxyl. A substantial conformational change observed upon binding of the inhibitor is a partial rearrangement of helix α9 (C3 of Figure 2). Residues 220−232 at the C-terminal end of this helix were more flexible in the unliganded enzyme, as judged by higher temperature factors and weaker electron density. Helix α9 rotates about its axis by approximately 10° and pivots around residue Glu 220, relocating toward the back of the core β-sheet. The loop connecting the C-terminal portion of α9 to the following helix α10 also undergoes a hinged movement toward the interior of the cavity. These combined movements bring the phenyl group of Tyr 225 inside the catalytic site cavity, enhancing the hydrophobic character of the nucleoside base binding site. Tyr 229 relocates above His 241 on top of the binding cavity, 4.2 Å from the aromatic ring of the inhibitor. Its side-chain hydroxyl group is directed toward the cavity which accommodates the purine ring of nucleoside substrates.

The loop connecting the C-terminal end of strand β3 to the crossover helix α3 (amino acids 78−83, C4 of Figure 2) was poorly defined in electron density maps of the unliganded IU-NH (*35*). In the structure of the complex with the pAPIR inhibitor, this loop is located on top of the active site, acting as a "lid". His 82 is 3.6 Å from the phenyl ring of the inhibitor, in proper orientation for a positive charge−π interaction (*45*). Similar cation−π interactions have been described in other systems, for example, the WSXWS box of extracellular cytokine receptors (*46, 47*), and is a stabilizing factor in these structures. Closing the "lid" also provides van der Waals contact between the methyl group of the isobutyl side chain of Ile 81 and the aromatic ring of the bound inhibitor.

Binding of the Transition-State Inhibitor. The refined conformation of bound pAPIR is not commonly observed in the structures of free, protein bound, or polymeric nucleosides or nucleotides, demonstrating that the enzyme forces an unusual geometric strain on the inhibitor. The iminoribitol ring of pAPIR adopts an uncommon C3′exo-C2′exo (C4′ endo) conformation with the major exo-configuration at C3′ (Figure 5). The phase angle P is 233°, and the puckering amplitude (*48*) is 36°. These values differ from the lowest energy conformations usually found in nucleosides. To test that the refined conformation of pAPIR was not biased by the initial model, the electron density of the inhibitor was fitted with both C2′-endo and C3′-endo initial conformations of the iminoribitol. In both cases, the final conformation of the inhibitor was C3′-exo after refinement.

The C3′-exo conformation is characteristic of the ribooxocarbenium ion transition state (*20*). The transition-state geometry results from the coordination of both the 2′ and 3′ hydroxyls to the calcium ion, and the O5′ oxygen by its hydrogen bonds to Glu 166 and Asn 160 (Figures 3, 4, and 6). Iminoribitol inhibitors bind to IU-NH with the imino nitrogen ($pK_a = 6.5$) in the unprotonated form (*25*). The

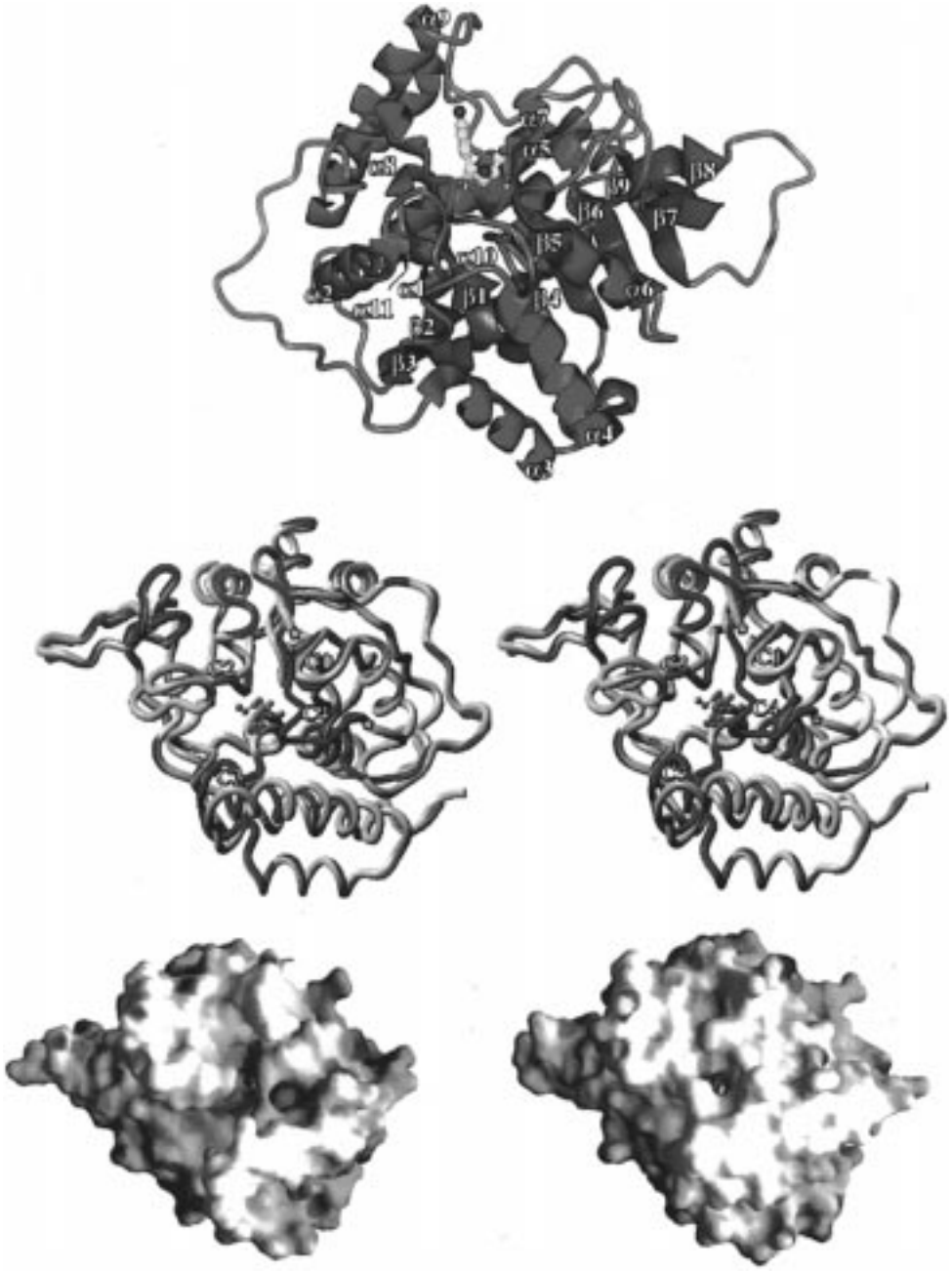

FIGURE 2: The ribbon structure of the IU-NH/pAPIR complex with strand assignments is shown in the upper panel. The fold of the enzyme is related to a Rossmann fold, with an open α,*β* structure. *β*-Strands are in blue, depicted as arrows, and α-helices in red. The strand identifiers are placed near the N-terminus of each strand. The inhibitor, bound at the C-terminal end of the core *β*-sheet, is shown as a ball-and-stick model. The figure was generated using Midas Plus 2.0 (*59*). Inhibitor-induced conformational changes in IU-NH (middle panel). A stereoview superposition of unliganded IU-NH (PDB accession code 1MAS, displayed as a gray tube) and the IU-NH/pAPIR complex (green tube). The regions of the protein secondary structure which relocate upon inhibitor binding are indicated in green. The loop C4 was not located in the native structure, and the ends of this region are marked with an asterisk (*). The conformational changes are localized in the active site area, bordered by strands *β*1, *β*4, and helices α9 and α10. The orientation of the enzyme in the upper and middle panels has been changed to best illustrate the structural features. The C1 change moves the loop connecting *β*2 and α2 to position Asn 39 near the inhibitor (Figure 3). The C2 changes brings aromatic residues from α5 into the catalytic site. Relocation of the entire α9-helix is indicated by C3. Unresolved residues from the loop between *β*3 and α3 in the unliganded structure appear above the catalytic site in the complex and are indicated as C4. The lower panel presents a view of the electrostatic potential of IU-NH with an empty catalytic site (left) and for the complex with pAPIR (right). Areas of negative and positive charge are red and blue, respectively. The centrally located positive potential surrounded by an area of negative potential is the Ca^{2+} surrounded by acidic residues. The inhibitor molecule (right) is almost completely enclosed by the protein as a result of the conformational change which accompanies binding. The figure was generated using GRASP (*56*).

2.5 Å hydrogen bond to Glu 166 is the shortest between the enzyme and inhibitor. The O5′-hydroxymethyl group is oriented toward the iminoribitol ring in a geometry which would stabilize a transition state oxocarbenium ion via the lone pair electrons from O5′ in a neighboring group interaction (*28*, *29*). The distance from O5′ to N4′ in the bound inhibitor is 2.7 Å. The dihedral angle O5′-C5′-C4′-O4′ of the bound inhibitor is near-eclipsed at 336°, relative to the average value of 233° for free nucleosides and nucleotides (*48*).

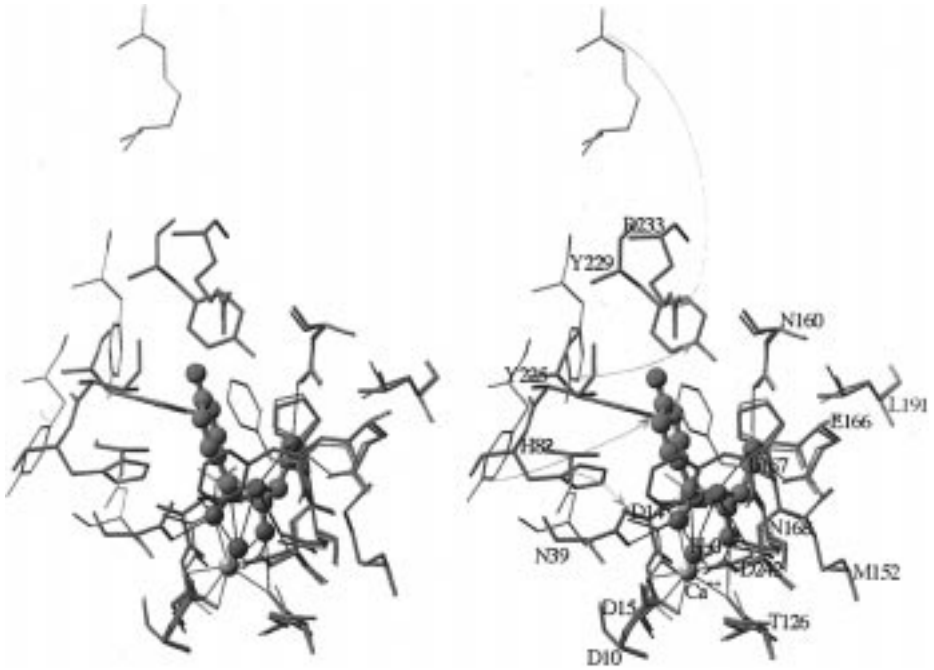

FIGURE 3: Stereoview of the conformational changes which occur in the catalytic site region of IU-NH in response to pAPIR binding. The backbones of the amino acids from the unliganded enzyme are indicated with thin bonds. Their repositioning in the complex of IU-NH/pAPIR is indicated by the arrows. The inhibitor is shown in a ball-and-stick model. Oxygens, including the Ca^{2+}-chelated water nucleophile are shown in red. The major hydrogen bond and metal chelate interactions are indicated by the black lines. Amino acids 166−168 remain near the same positions in the unliganded and filled site while side chains surrounding the p-aminophenyl group change substantially.

Structural Basis for Substrate Recognition. The leaving-group specificity for IU-NH includes all commonly occurring nucleosides, purine riboside, and *p*-nitrophenylribose but recognition of the ribosyl group is stringent, since the enzyme is catalytically inactive with 2′, 3′ or 5′ deoxyribopurines, and with mono-, di-, or triphosphonucleotides (*27, 30*). Binding of pAPIR results in the formation of at least nine hydrogen bonds and two metal chelate interactions to the iminoribitol moiety of the inhibitor but only one cation−π interaction and van der Waals contacts to the aniline ring (Figures 3, 4, and 6). Nucleosides which lack the 2′ or 3′ hydroxyls are expected to lose two hydrogen bonds and the bidentate chelate interaction to the calcium ion. Lack of the 5′ hydroxyl causes loss of the 2.5 Å hydrogen bond to Glu 166, the 3.0 Å contact to Asn 160 and the 2.7 Å neighboring group interaction between the 5′-hydroxyl and the oxocarbenium ion of the transition state. These are crucial interactions for catalysis since 5′-deoxynucleosides are not substrates (*27*). Substrates phosphorylated at the 5′-position cannot be accommodated because of the restricted active-site volume and the unfavorable electrostatic potential. The broad specificity for the leaving group results from the paucity of amino acids to form specific interactions. Tyr 229, His 82, and His 241 are the only residues in the leaving group site likely to form such interactions, and Tyr 229 is on one of the flexible loops. His 241 has been demonstrated to be involved in leaving-group activation in the hydrolysis of inosine, presumably as the proton donor for hypoxanthine (*34*). The residual activity (10^{-3}) of the His 241 Ala mutant could occur from an alternate proton donor, possibly His 82. However, the activation of ribose is the most important catalytic force for IU-NH (*25, 30*).

A Novel Calcium Interaction at the Catalytic Site of IU-NH. The enzyme−inhibitor complex reveals a calcium ion bound between the cluster of acidic residues in the active site (Figures 3−5). This electron-dense ion was present in the unliganded enzyme but was assigned as potassium based on its hexacoordination and the presence of 0.3 M K^+ in the crystallization medium (*35*). In the native enzyme, the six ligands are provided by carboxyl contacts from Asp 15, Asp 242, and Asp 10 and the main-chain carbonyl of Thr 126 together with one ordered water. In the complex with inhibitor, the metal is coordinated by eight oxygens, with the two additional ligands contributed by the 2′ and 3′ hydroxyls of bound inhibitor. Octacoordination by oxygen is the most common chelate scheme for Ca^{2+} in the Cambridge Structure Database for small molecules and is also the most common in proteins from the Protein Data Bank (*49*). The distances between the ion and its ligands are summarized in Table 2 and are compared to the distances for the metal ion in unliganded IU-NH. Plasma emission spectroscopic analysis confirmed that a near-stoichiometric amount of calcium is bound to IU-NH. The Ca^{2+} is tightly bound, since the initial reaction rate of IU-NH catalytic

Table 2: Comparison of Ligands to Ca^{2+} in Native IU-NH and with Bound pAPIR

ligand	Å distances		structural contact[a]
	native	pAPIR complex	
O2′	none	2.5	inhibitor
O3′	none	2.5	inhibitor
Thr 126 O	2.7	2.3	β4
Asp 242 OD2	2.5	2.6	α10
Asp 10 OD1	2.5	2.5	loop β1-α1
Asp 15 OD1	2.5	2.5	α1
Asp 15 OD2	2.7	2.6	α1
H_2O	2.4	2.4	O-nucleophile

[a] Protein contacts to bound Ca^{2+} are indicated as sequential β-sheet and α-helix elements numbered from the N-terminal. Loop β1-α1 refers to a short loop connecting these sequences. In the native structure the Ca^{2+} is hexacoordinate.

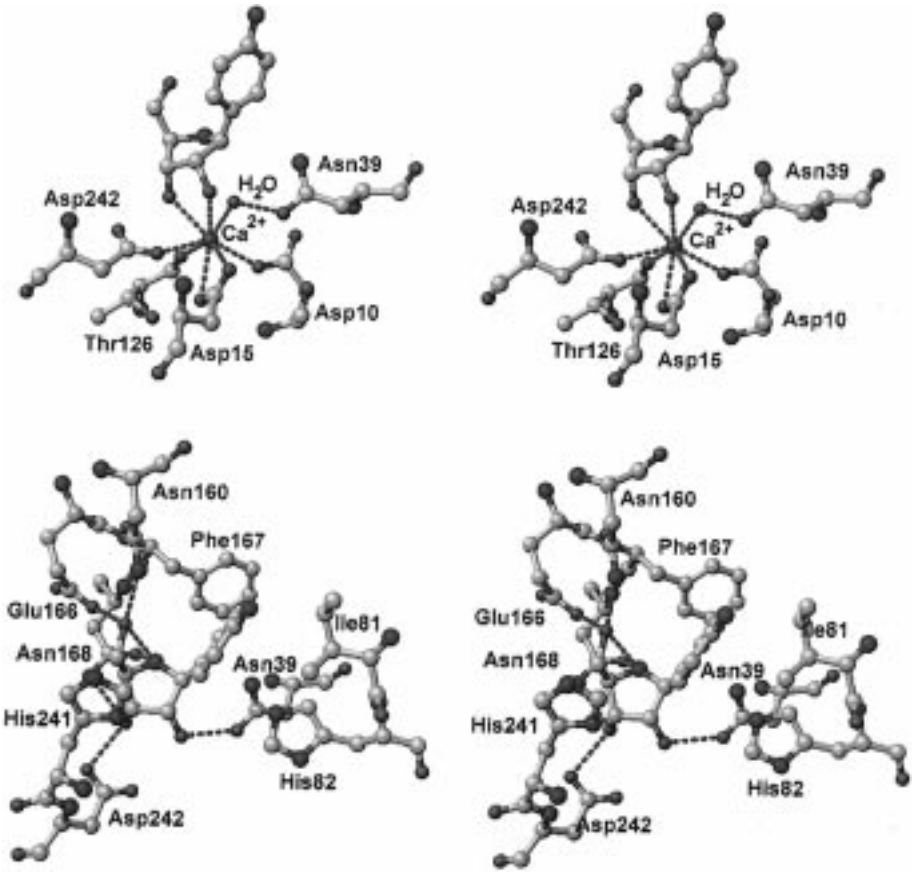

FIGURE 4: Stereoviews of the interactions between the enzyme, Ca^{2+} and transition-state inhibitor. The upper panel is a stereoview of the ligands to the Ca^{2+} ion in the enzyme−inhibitor complex. The view demonstrates the octacoordination geometry of the metal ion. The sole coordinated water molecule is 3.2 Å from C1′ of the iminoribitol and is the only candidate for the incipient nucleophile in the transition state. The lower panel indicates amino acid interactions with the inhibitor. Hydrogen bonds to the iminoribitol group of the inhibitor are drawn as dashed lines. The interactions with the aniline ring of the inhibitor are hydrophobic with the exception of the His 82−π system interaction. The distance of the NE1 atom of His 82 to the center of the aromatic ring is 3.6 Å. The figure was generated using Midas Plus 2.0 (*59*).

activity is not inhibited by the presence of 10 mM EGTA in the reaction mixture. Extensive incubation with EGTA causes loss of activity which can be restored by addition of Ca^{2+} in assay mixtures (V. L. Schramm, unpublished material).

The Ca^{2+}-chelated water is located 2.4 Å from Ca^{2+} and 3.2 Å from C1′ of the inhibitor with polar contacts to Asn 39 (2.5 Å) and Asp 10 (2.9 Å) (Figures 3-5). Activation of the water nucleophile in IU-NH could occur by the Ca^{2+}−H_2O interaction to decrease the pK_a for the bound water, followed by proton transfer to the carboxyl oxygen of Asp 10 as the incipient hydroxyl ion attacks, following formation of the ribosyl-oxocarbenium ion. Kinetic studies with the Asp 10 Ala mutant support this assignment for the general base (*50*). The Ca^{2+}-bound water molecule is in the appropriate geometry to attack C1′ after the ribooxocarbenium ion has been formed. The calcium ion of IU-NH also aligns the carboxylate side chain of Asp 10 in a position to accept a proton from the bound water, and constrains the 2′ and 3′ hydroxyls of iminoribitol in an orientation that stabilizes an oxocarbenium ion conformation for a ribosyl group. The only other conclusive report of a calcium ion which directly activates a water molecule for catalysis is the staphylococcal nuclease from *S. aureus,* although other enzymes (e.g., phospholipase A2 and lysosomal sulfatase) use Ca^{2+} for geometric organization at the catalytic site (*51, 52*). The calcium-binding site of IU-NH is unique by interacting with protein residues from distributed structural elements of the protein. Asp 10 is located in a short loop connecting strand β1 to helix α1. Asp 15 is in the first turn of helix α1; Thr 126 is in the middle of strand β4 and Asp 242 is the N-terminal residue of helix α10. In phospholipase A2, the calcium is heptacoordinated, with two water molecules as part of the coordination sphere. The interaction with one aspartate residue is bidentate, and three main-chain carbonyl oxygens, separated each by one amino acid residue, form a characteristic Ca^{2+} binding loop in a distorted bipyramidal coordination. In staphylococcal nuclease, three coordination sites are filled by protein atoms, including one main chain carbonyl and two side-chain carboxylates. Three water molecules and an oxygen from the bound substrate complete the heptacoordination. The protein residues in the nuclease come from two distinct loop regions of the structure with Asp 21 coordinating the calcium and the water molecule that is proposed to attack the substrate. In the classic EF hand, calcium ion is coordinated by residues from a semicircular loop connecting two α-helices. In calmodulin, this motif is 11 residues long with two aspartate and one glutamate carboxylate as well as a threonine main-chain carbonyl to bind the Ca^{2+} (*54, 55*). The average protein−Ca^{2+} distances are comparable for all three enzymes, at 2.6 Å. The Ca^{2+}−nucleophilic H_2O bonds of both IU-NH and staphylococcal nuclease are 2.4 Å, reflecting stronger interactions to provide water activation. In these three

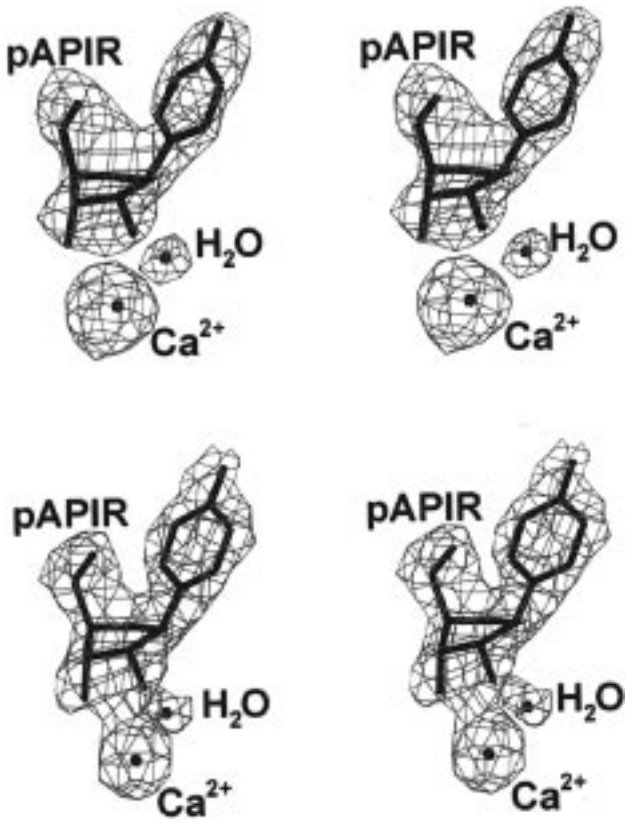

FIGURE 5: Stereoview of the electron density and the model for the inhibitor, calcium and catalytic water (upper panel). Shown in red is the electron density map, calculated with SIGMAA-weighted $F_o - F_c$ coefficients and phases from the model after molecular replacement and rigid body refinement to 2.5 Å resolution. Electron density is contoured at 3σ. At this stage of the structural analysis, the inhibitor, ion and water, shown in black, had not been included in the model. Final electron density (lower panel), calculated from SIGMAA-weighted $2F_o - F_c$ coefficients after omitting the inhibitor, Ca^{2+} ion and water molecule, contoured at 1σ. The inhibitor geometry was established from a crystallographic refinement in which only bond lengths, bond angles, and the chiralities that define a β-D-nucleoside were restrained. The figure was generated using the program TOM, a derivative of FRODO (*60*).

examples, Ca^{2+} is located in a crevice near the protein surface. In IU-NH, the ion is at the bottom of a deep cavity. This shields the reaction center from bulk solvent and fosters the tight interactions clustered about the Ca^{2+}. Solvent access to the C1′ atom of the bound iminoribitol moiety was calculated using GRASP (*56*) and a spherical probe of 1.7 Å radius. The accessible surface for the C1′ atom using this probe is 0.0 Å^2, indicating no solvent access.

Transition State Stabilization. Features of actual enzymatic transition states are not directly available from spectroscopic or structural approaches but can be deduced from kinetic isotope effects (*57*). The structure of inosine at the transition state of IU-NH has been established by this method and used to design transition-state inhibitors, including pAPIR (*26, 28, 29*). Comparison of the transition-state features for inosine, predicted from the isotopic studies, can now be directly compared in the crystal stucture with bound pAPIR. The protein contacts which play a role in stabilizing the transition state also cause the tight binding observed with pAPIR, since the pH profiles for the binding of iminoribitol analogues is equivalent to that for k_{cat} and do not correspond to pH profiles for substrate binding (*25, 58*). The tight binding of this inhibitor (K_m/K_i is approximately 10^4) also suggests transition-state interactions. The transition state for hydrolysis of inosine has the features (a) neutral, planar hydrophobic leaving group caused by proton donation to the leaving group using His 241 as the general acid; (b) a flattened, positively charged ribooxocarbenium ion with sp^2-hybridized C1′ and C3′-exo geometry; (c) distortion of the 5′-hydroxymethyl group to place the 5′-hydroxyl over the ribose ring; and (d) an enzyme-activated water molecule is 3.0 Å from C1′ and is distinct from bulk solvent water molecules (*20, 28*).

Each of these transition-state features is reflected in the crystal structure with bound pAPIR: (a) The aniline group is in a pocket surrounded by hydrophobic residues, which cluster to the site as a consequence of inhibitor binding. The unfavorable pK_a of the aniline group prevents protonation. The hydrophobic pocket has few residues which can interact specifically with substrates and accounts for the broad leaving-group specificity of IU-NH. (b) An sp^2-hybrization at C1′ predicts a ribose C3′-exo conformation, with C3′ below the plane of the ring. In free inosine, the C3′-endo puckering, with C3′ above the plane of the ribose ring, is favored. Even though C1′ of pAPIR is covalently locked in sp^3 conformation, the enzyme forces the sugar pucker toward C3′-exo, using the numerous hydrogen bonds and constraining the 2′ and 3′-hydroxyls in the Ca^{2+} octacoordination geometry. (c) Positioning of the 5′-hydroxyl to within 2.7 Å of N4′ of the iminoribitol establishes an unusual ribosyl geometry, indicating neighboring-group participation of the 5′-oxygen lone pair being directed toward the positive charge of the oxocarbenium ion. (d) the observed C1′-water oxygen distance of 3.2 Å is close to the predicted 3.0 Å from kinetic isotope effects. The Ca^{2+}-bound water is surrounded by protein with no access for bulk solvent to the ribosyl C1′ atom. At the transition state, the H_2O is not yet ionized, but is converted to the hydroxyl ion after transition state formation, based on solvent isotope effects (*20, 28*). It is assumed that H_2O rather than hydroxide ion is bound at the catalytic site in the pAPIR structure. The most likely candidate for the subsequent ionization of H_2O is Asp 10. Activation of H_2O by Ca^{2+} is unusual for hydrolases and was not predicted for IU-NH until the ion was located by crystallography.

Most of the binding energy for pAPIR resides in the iminoribitol contacts (*25, 29*). Of these, the two bifurcated hydrogen bonds are of note (Figures 3 and 6), as are the multiple Ca^{2+} interactions. The H-bonding pattern implicated in Figure 4 has the 5′-hydroxyl as a H-bond donor to Glu166 and H-bonds to the 5′-oxygen from the imino nitrogen and Asn 160. The imino nitrogen also is a H-bond donor to Asn168 suggesting a formal charge of +1 for the iminoribitol, similar to that of the transition state. This conclusion does not agree with the pH profiles which are consistent with binding of unprotonated iminoribitols (*25, 28*). More direct methods will be necessary to resolve this discrepancy.

Although the 30 nM binding constant greatly exceeds that of the substrate, it is far from the hypothetical limit of 10^{-16} M for the perfect transition-state inhibitor for IU-NH (*29*). Perfection in transition-state inhibitors has not been achieved because of the need for chemical stability and the difficulty in matching nonequilibrium bond lengths. Fortunately, capturing only a small fraction of transition state binding

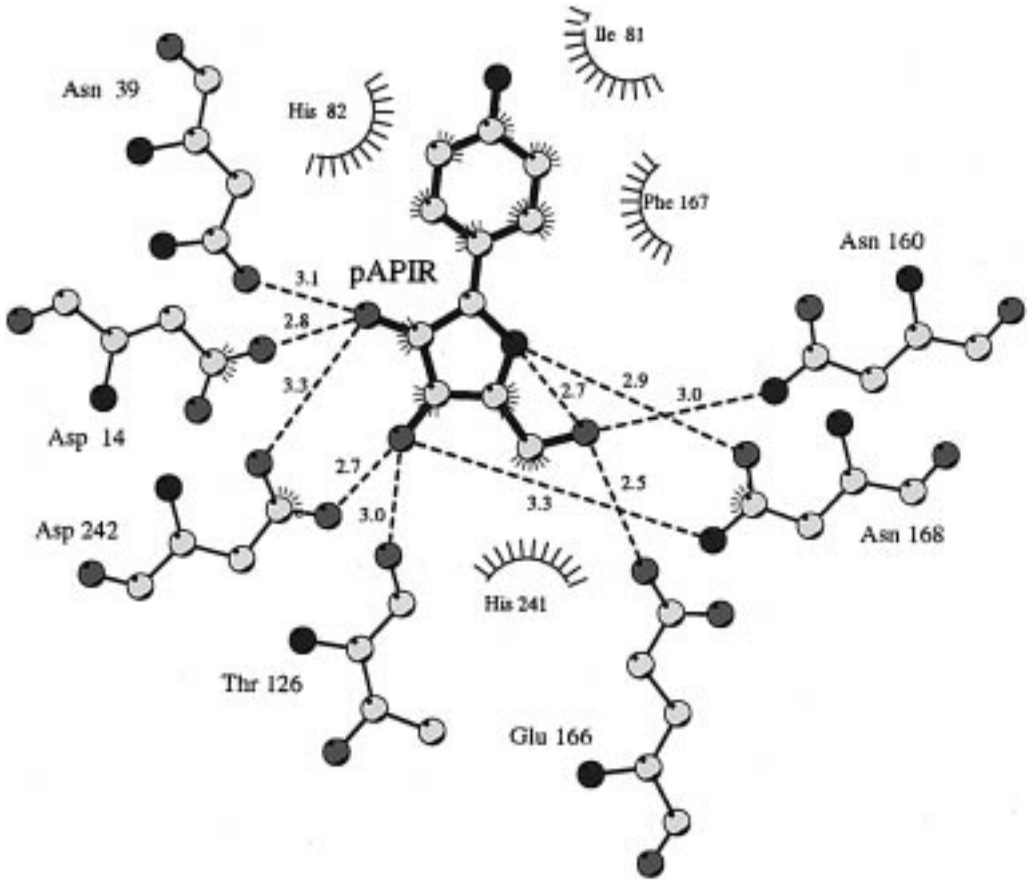

FIGURE 6: A two-dimensional map of the distances for contacts between the enzyme and the bound transition-state inhibitor. In the unliganded enzyme Asp 14 is hydrogen bonded to His 241. These groups separate when inhibitor binds and the enzyme undergoes the conformational changes shown in Figure 2. The highlighted residues indicate van der Waals contact, and dashed lines indicate H bonds with the indicated distances. Interactions with Ca^{2+} are shown in Figures 3 and 4. Hydrogen bond and van der Waals contacts were calculated using HBPLUS (*61*) and the plot generated with LIGPLOT 2.0 (*62*).

energy still provides powerful inhibitors (*57*). Knowledge of the interactions of pAPIR with the enzyme provides access to additional improvements in nucleoside hydrolase inhibitors.

Implications for Rational Inhibitor Design. An applied interest in the nucleoside hydrolases resides in the essential pathway of purine salvage for the life cycle of protozoan parasites. Inhibitors of nucleoside hydrolases have been considered as antiprotozoan agents since mammals rely primarily on de novo synthesis of purines and lack nucleoside hydrolase activity. Nucleobases are salvaged in mammals by phosphoribosyl transferases, which have structural and catalytic properties distinct from nucleoside hydrolases. Analogues to 2 nM inhibitor constants have been designed on the basis of the transition-state structure; however, the most powerful are chemically unstable (*31*, *32*). The availability of the three-dimensional structure of the enzyme with a bound pAPIR should permit a rational modification of these inhibitory ligands.

The 4′-imino group is responsible for much of the binding energy for the iminoribitol inhibitors, and the close packing of residues around this group make it unlikely that large changes would be tolerated. However, sp^2 hybridization at C1′ would favor the observed ribosyl pucker and is known to improve binding in the case of *p*-nitrophenylriboamidrazone, a transition-state inhibitor with a 2 nM dissociation constant (*32*). The crystal structure reveals numerous groups in the leaving-group pocket which have not been exploited in inhibitor design. Thus, Arg 233, Tyr 229, His 82, Tyr 225, and His 241 are all candidates for hydrogen bond or hydrophobic interactions within reach of the leaving group cavity. The dramatic relocation of Arg 233, Tyr 225, and Tyr 229 upon inhibitor binding are of special note. Incorporation of groups which interact with these flexible groups around the catalytic site offer a strong possibility of increasing the binding energy.

Conclusions. The structure of IU-NH with pAPIR demonstrates a novel mechanism for ribohydrolases by establishing a Ca^{2+}-bound water at the catalytic site. The basis for substrate specificity is established from the flexible and hydrophobic nature of amino acids in the leaving-group pocket. Transition-state features from physical-chemical approaches are closely correlated to that found in the structure with bound transition-state inhibitor. Features which can be targeted for improved inhibitor design are apparent from the structure.

ACKNOWLEDGMENT

The authors thank Drs. R. N. Furneaux and P. C. Tyler, Industrial Research Limited, New Zealand for providing the pAPIR; Drs. D. N. Gopaul and O. Varlamova for providing enzyme and the metal analysis; and Drs. P. J. Berti and G. Scapin for help with figure preparation and useful comments on the manuscript. Dr. Ian Wilson is thanked for his critical evaluation of the work and use of the graphic and computational facilities at the Scripps Research Institute. The

coordinates have been deposited with the Protein Data Bank under the accession code 2MAS and are available from the authors prior to release (e-mail: massimo@scripps.edu).

REFERENCES

1. Sancar, A., and Sancar, G. B. (1988) *Annu. Rev. Biochem. 57*, 29−67.
2. Romier, C., Reuter, K., Suck, D., and Ficner, R. (1996) *Biochemistry 35*, 15734−15739.
3. Hammond, D. J., and Gutteridge, W. E. (1984) *Mol. Biochem. Parasitol. 13*, 243−261.
4. Miller, R. L., Sabourin, C. L. K., Krenitsky, T. A., Berens, R. L., and Marr, J. J. (1984) *J. Biol. Chem. 265*, 5073−5077.
5. Endo, Y., Gluck. A., and Wool, I. G. (1991) *J. Mol. Biol. 221*, 193−207.
6. Monzingo, A. F., and Robertus, J. D. (1992) *J. Mol. Biol. 227*, 1136−1145.
7. Aktories, K. Ed. (1992) *Current Topics in Microbiology and Immunology. ADP−Ribosylating Toxins*; Springer-Verlag; Berlin.
8. Lee, H. C., Galione, A., and Walseth, T. F. (1994) *Vitam. Horm. 48*, 199−257.
9. Erion, M. D., Takabayashi, K., Smith, H. B., Kessi, J., Wagner, S., Hönger, S., Shames, S. L., and Ealick, S. E. (1997) *Biochemistry 36*, 11725−11734.
10. Kline, P. C., and Schramm, V. L. (1992) *Biochemistry 31*, 5964−5973.
11. Mao, C., Cook, W. J., Zhou, M. Koszalka, G. W., Krenitsky, T. A., and Ealick, S. E. (1997) *Structure 5*, 1373−1383.
12. Bell, C. E., and Eisenberg, D. (1996) *Biochemistry 35*, 1137−1149.
13. Ealick S. E., Rule, S. A., Carter, D. C., Greenhough, T. J., Babu, Y. S., Cook, W. J., Habash, J., Helliwell, J. R., Stoeckler, J. D., Parks, R. E., Jr., Chen, S. F., and Bugg, C. E. (1990) *J. Biol. Chem. 265*, 1812−1820.
14. Zhang, R. G., Scott, D. L., Westbrook, M. L., Nance, S., Spangler, B. D., Shipley, G. G., and Westbrook, E. M. (1995) *J. Mol. Biol. 251*, 563−573.
15. Stein, P. E., Boodhoo, A., Armstrong, G. D., Cockle, S. A., Klein, M. H., and Read, R. J. (1994) *Structure 2*, 45−57.
16. Savva, R., McAuley-Hecht, K., Brown, T., and Pearl, L. (1995) *Nature 373*, 487−493.
17. Armstrong, S. R., Cook, W. J., Short, S. A., and Ealick, S. E. (1996) *Structure 4*, 97−107.
18. Mol, C. D., Arvai, A. S., Slupphaugh, G., Kavli, B., Alseth, I., Krokan, H. E., and Tainer, J. A. (1995) *Cell 80*, 869−878.
19. Mentch, F. Parkin, D. W., and Schramm, V. L. (1987) *Biochemistry 26*, 921−930.
20. Horenstein, B. A., Parkin, D. W., Estupiñán, B., and Schramm, V. L. (1991) *Biochemistry 30*, 10788−10795.
21. Kline, P. C., and Schramm, V. L. (1993) *Biochemistry 32*, 13212−13219.
22. Scheuring, J., and Schramm, V. L. (1997) *Biochemistry 36*, 8215−8223.
23. Rising, K. A., and Schramm, V. L. (1997) *J. Am. Chem. Soc. 119*, 27−37.
24. Berti, P. J., Blanke, S. R., and Schramm, V. L. (1997) *J. Am. Chem. Soc. 119*, 12079−12088.
25. Parkin, D. W., Limberg, G., Tyler, P. C., Furneaux, R. H., Chen, X.-Y., and Schramm, V. L. (1997) *Biochemistry 36*, 3528−3534.
26. Furneaux, R. N., Limberg, G., Tyler, P. C., and Schramm, V. L. (1997) *Tetrahedron 53*, 2915−2930.
27. Parkin, D. W., Horenstein, B. A., Abdulah, D. R., Estupiñán, B., and Schramm, V. L. (1991) *J. Biol. Chem. 266*, 20658−20665.
28. Horenstein B. A., and Schramm, V. L. (1993) *Biochemistry 32*, 9917−9925.
29. Horenstein, B. A., and Schramm, V. L. (1993) *Biochemistry 32*, 7089−7097.
30. Mazzella, L. J., Parkin, D. W., Tyler, P. C., Furneaux, R. H., and Schramm, V. L. (1996) *J. Am. Chem. Soc. 118*, 2111−2112.
31. Deng, H., Chan, A. W.-Y., Bagdassarian, C. K., Estupiñan, B., Ganem, B., Callender, R. H., and Schramm, V. L. (1996) *Biochemistry 35*, 6037−6047.
32. Boutellier, M., Horenstein, B. A., Semenyaka, A., Schramm, V. L., and Ganem, B. (1994) *Biochemistry 33*, 3994−4000.
33. Pellé, R., Schramm, V. L., and Parkin, D. W. (1998) *J. Biol. Chem. 273*, 2118−2126.
34. Gopaul, D. N., Meyer, S. L., Degano, M., Sacchettini, J. C., and Schramm, V. L. (1996) *Biochemistry 35*, 5963−5970.
35. Degano, M., Gopaul, D. N., Scapin, G., Schramm, V. L., and Sacchettini, J. C. (1996) *Biochemistry 35*, 5971−5981.
36. SAINT, SAINT Reference Manual, Siemens Energy & Automation Inc. Madison, WI (1996).
37. Navaza J. (1994) *Acta Crystallogr., Sect.* A *50*, 157−163.
38. CCP4, The Collaborative Computational Project Number 4 suite: programmes for protein crystallography. (1994). *Acta Crystallogr., Sect.* D *50*, 760−763.
39. Brünger, A. T. (1992) *Nature 35*5, 472−474.
40. Brünger, A. T., Kuryian, J., and Karplus, M. (1987) *Science 235*, 458−460.
41. Read, R. J. (1986) *Acta Crystallog., Sect.* A *42*, 140−149.
42. Jones, T. A., Zou, J.-Y., and Cowan, S. W. (1991) *Acta Crystallogr.; Sect.* A *47*, 110−119.
43. Laskowski, R. A., MacArthur, M. W., Moss, D. S., and Thornton, J. (1993) *J. Appl. Crystallogr. 26*, 283−291.
44. Kleywegt, G. J., and Brünger, A. T. (1996) *Structure 4*, 897−904.
45. Burley, S. K., and Petsko, G. A. (1988) *Adv. Protein Chem. 39*, 125−189.
46. deVos, A. M., Ultsch, M., and Kossiakoff, A. A. (1992) *Science 225*, 306−312.
47. Livnah O., Stura, E. A., Johnson, D. L., Middleton, S. A., Mulcahy, L. S., Wrighton, N. C., Dower, W. J., Jolliffe, L. K., and Wilson, I. A. (1996) *Science 273*, 464−471.
48. Gelbin, A., Schneider, B., Clowney, L., Hsieh, S. H., Olson, W. K., and Berman, H. M. (1996) *J. Am. Chem. Soc. 118*, 519−529.
49. Katz, A. K., Glusker, J. P., Beebe, S. A., and Bock, C. W. (1996) *J. Am. Chem. Soc. 118*, 5752−5763.
50. Gopaul, D. N. (1996) Ph.D. Thesis, Albert Einstein College of Medicine of Yeshiva University, Bronx, N. Y.
51. Loll, P. J., Quirk, S., Lattman, E. E., and Garavito, R. M. (1995) *Biochemistry 34*, 4316−4324.
52. Scott, D. L., White, S. P., Otwinowski, Z., Yuan, W., Gelb, M. H., and Sigler, P. B. (1990) *Science 250*, 1541−1546.
53. Bond, C. S., Clements, P. R., Ashby, S. J., Collyer, C. A., Harrop, S. J., Hopwood, J. J., and Guss, J. M (1997) *Structure 5*, 277−289.
54. Wang, X. Q., Yang, J., Gui, L. L., Lin, Z. J., and Zhou, Y. C. (1996) *J. Mol. Biol. 255*, 669−676.
55. Chattopadhyaya, R., Meador, W. E., Means, A. R., and Quiocho, F. A. (1992) *J. Mol. Biol. 288*, 1177−1192.
56. Nicholls, A., Sharp K. A., and Honig, B. (1991) *Proteins: Struct., Funct., Genet. 11*, 281−296.
57. Schramm, V. L., Horenstein, B. A., and Kline, P. C. (1994) *J. Biol. Chem. 269*, 18259−18263.
58. Parkin, D. W., and Schramm, V. L. (1995) *Biochemistry 34*, 13961−13966.
59. Ferrin, T. E., Huang, C. C., Jarvis, L. E., and Langridge, R. (1988) *J. Mol. Graphics 6*, 13.
60. Jones, T. A. (1985) *Methods Enzymol. 115*, 157−171.
61. McDonald, I. K., and Thornton, J. M. (1994) *J. Mol. Biol. 238*, 777−793.
62. Wallace, A. C., Laskowski, R. A., and Thornton, J. M. (1995) *Protein Eng. 8*, 127−134.

BI973012E